ChemComm

ROYAL SOCIETY OF CHEMISTRY

COMMUNICATION

View Article Online
View Journal | View Issue

Cite this: *Chem. Commun.*, 2025, **61**, 4694

Received 6th October 2024,
Accepted 30th January 2025

DOI: 10.1039/d4cc05129g

rsc.li/chemcomm

Controlled acidity-mediated short-chain olefin synthesis over a Mn–Zn–Zr/Zn-SAPO-34 catalyst *via* CO_2 hydrogenation†

Gaje Singh,[ab] Satyajit Panda,[ab] Vivek Kumar Shrivastaw[ab] and Ankur Bordoloi *[ab]

Transforming CO_2 into short-chain olefins *via* a methanol-mediated route is challenging due to CO byproduct formation. This study introduces a Mn–Zn–Zr/Zn-SAPO-34 catalyst, achieving 81% short-chain olefin selectivity, 3.9% methane, and 65% CO formation with 18% CO_2 conversion. This research demonstrates an effective bifunctional catalyst design for direct CO_2 hydrogenation into valuable hydrocarbons.

To meet the increasing energy demand, the widespread use of fossil fuels has substantially increased greenhouse gas (GHG) emissions, exacerbating climate change.[1] Additionally, short-chain olefins, which are fundamental building blocks in the petrochemical industry and responsible for materials of regular usage in our day-to-day life, are still dependent on crude oil and release a significant amount of CO_2 during their conventional production.[2] In this instance, the increasing demand for short-chain olefins and the steadily rising CO_2 emissions levels become incompatible, necessitating a prompt solution. The CO_2 hydrogenation to short-chain olefins is one of the popular approaches for reducing CO_2 emission levels and simultaneously limits the dependency on fossil fuels.[3]

There are mainly two pathways for the synthesis of short-chain olefins; (i) modified Fischer Tropsch synthesis (MFTS) utilizing iron-based catalysts and (ii) oxide/zeolite-based catalysts *via* methanol as an intermediate product.[3] The MFTS route forms an alkyl chain that separates from the active sites following hydrogenation and beta-H abstraction, producing paraffin and olefins. The distribution of alkyl chain length is determined by the Anderson–Schulz–Flory (ASF) distribution, which limits the C_2–C_4 olefin range, which is less than 60% in hydrocarbons.[4] Unlike the MFTS method, the methanol-mediated route does not have the constraints of the ASF distribution and is primarily focused on C_2–C_4 hydrocarbons. The chemical pathway includes CO_2 hydrogenation to methanol and the subsequent transformation of methanol to hydrocarbon. As a result, the synthesis of a methanol intermediate serves as a key link between the two processes described above. By virtue of these reaction properties, we can make a bifunctional metal oxides-zeolite-based catalyst appropriate for this pathway, in which metal oxides catalyze CO_2 to produce methanol. Then, zeolites transform methanol into olefins by a C–C coupling process.[5]

Among the non-noble metal-based catalysts, Cu-based catalysts have been developed and utilized on a large scale for CO_2 hydrogenation to methanol.[6] However, Cu-based catalysts are often deactivated at high temperatures (>300 °C), an obvious temperature necessary for methanol dehydration to olefins over zeolite acidic sites. As a result, Cu-free catalysts, particularly spinel oxides, mixed binary oxides, and ternary oxides-based catalysts such as ZnO–ZrO_2, In_2O_3–ZrO_2, In_2O_3–$ZnZrO_x$, and $ZnGa_2O_4$, have recently been explored and implemented for the synthesis of methanol.[7] These catalysts possess good reaction performance and stability for CO_2 hydrogenation to methanol at higher temperatures (>300 °C). In this strategy, an ideal temperature can be attained for both reaction steps of CO_2 hydrogenation to olefins *via* the methanol-mediated route.

The zeolite component of the bifunctional catalyst plays an important role in methanol conversion *via* C–C coupling reaction. Acidic zeolites, such as HZSM-5 (hydrogen-form Zeolite Socony Mobil–5) and SAPOs (silicoaluminophosphates), are commonly utilized due to their optimal acidity and shape selectivity.[8] HZSM-5 zeolite features an MFI framework, known for its three-dimensional network of intersecting channels and medium-sized pores measuring roughly 0.55 nm in diameter. On the other hand, SAPOs exhibit a range of structural types that resemble those of zeolites. These structures can include CHA (chabazite), AEL (aluminophosphate type), or AFI (aluminophosphate type I) frameworks. The specific structural type of a SAPO affects its catalytic properties and pore dimensions, which typically vary from small to medium sizes, approximately 0.3 to 0.7 nm. The SAPO-34 zeolite outperforms other zeolites

[a] *Light and Stock Processing Division, CSIR-Indian Institute of Petroleum (IIP), Dehradun-248005, India*
[b] *Academy of Scientific and Innovative Research (AcSIR), Ghaziabad-201002, India*

† Electronic supplementary information (ESI) available. See DOI: https://doi.org/10.1039/d4cc05129g

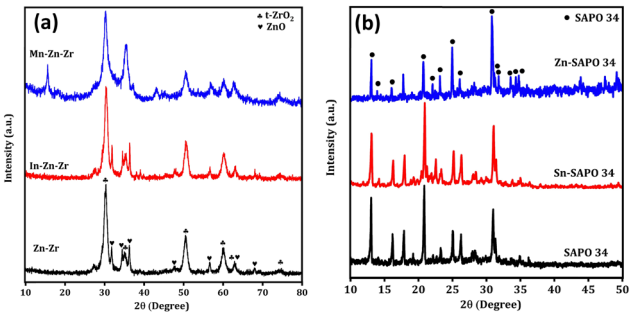

Fig. 1 XRD patterns of the ZnO–ZrO_2 oxides (a) and SAPO-34 catalysts (b).

with outstanding catalytic performance due to its smaller pore size (0.38 nm), peculiar framework with a CHA cage (9.4 Å), excellent thermal stability, and adequate acidity, which promotes the synthesis of short-chain olefins.[9] Furthermore, one popular strategy for improving the thermal stability and selectivity of C_2 and C_3 olefins is to modify SAPO-34 with transition metals (Zn, Mn, Co, Cr, *etc.*).

Here, modified ZnO–ZrO_2 oxide-based catalysts and modified (Zn or Sn) SAPO-34 zeolite were developed for the direct and selective transformation of CO_2 to short-chain olefins, linking methanol production and subsequent dehydration to short-chain olefins.

The ESI† contains detailed descriptions of the catalyst synthesis, characterization techniques, and activity testing procedures.

XRD analysis was performed to characterize the crystal structures of all prepared samples. Fig. 1a displays the XRD profiles of the calcined ZnO–ZrO_2 oxide-based catalysts. The diffraction patterns of the samples showed distinct peaks at 31.80, 34.40, 36.20, and 56.7° (2θ), corresponding to the (100), (002), (101), and (110) crystal planes, respectively. These diffraction peaks align perfectly with the typical ZnO hexagonal wurtzite-type structure (JCPDS 36-1451).[10,11] On the other hand, the slightly broad diffraction peaks at 30.3, 35.2, 50.6, 60.0, 62.9, and 74.3° are associated with the (101), (110), (112), (211), (202), and (220) crystal planes of the tetragonal ZrO_2 phase (t-ZrO_2, JCPDS cards no. 79-1771).[12] The *t*-ZrO_2 phase is a widely reported phase of ZrO_2 when the catalyst material is calcined at 500 °C.[13] Overall the XRD results suggest the successful formation of the ZnO–ZrO_2 oxide catalysts.

Fig. 1b shows the XRD pattern of the SAPO-34 and modified (Sn/Zn) SAPO-34 catalysts. The diffraction peaks of all the samples matched well with the SAPO-34 chabazite (CHA) phase with the space group of $R\bar{3}m$.[14] The diffraction pattern of modified SAPO-34 shows that the CHA structure and crystal phase of SAPO-34 molecular sieves remain unchanged and had no discernible effect following the inclusion of the Sn and Zn species. No Sn or Zn crystal phases were observed, either due to a low concentration or high dispersion of these species, because the peaks were obscured by the highly crystalline diffraction peaks of the SAPO-34 phase.

Fig. 2a and b depict the SEM image of the Zn-SAPO-34 molecular sieve catalyst. The figures exhibit the typical cubic crystal shape of SAPO-34 with a well-ordered and smooth

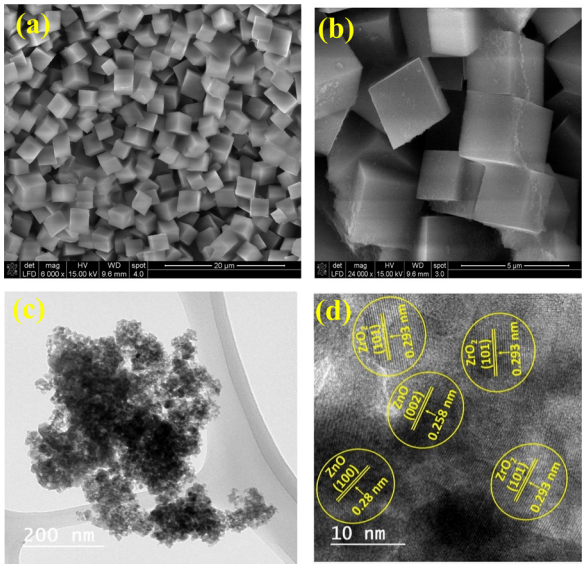

Fig. 2 FESEM images (a) and (b) of the Zn-SAPO-34 catalyst and TEM images of the Mn–Zn–Zr catalyst (c) and (d).

particle size of around 2.5 μm. In Fig. S1 (ESI†), SEM-EDS spectra demonstrate that all component elements (Zn, Si, Al, P, and O) are present in Zn-SAPO-34 and are free of other impure elements. The morphology and nanostructure of the Mn–Zn–Zr oxides catalyst were further characterized by TEM, HRTEM, and selected area electron diffraction (SAED) pattern, as shown in Fig. 2c. The examination of the TEM images presented in Fig. 3c and d reveals that the particles are slightly agglomerated and have well-defined lattice fringes. Fig. 2d shows a lattice spacing of 0.293 nm, corresponding to the *d*-spacing of the (101) crystal plane in tetragonal ZrO_2. Similarly, the *d*-spacing of the (100) and (002) crystal planes of the ZnO hexagonal wurtzite structure results in lattice spacing of 0.28 nm and 0.258 nm, respectively. These findings were consistent with their corresponding XRD diffraction pattern as the *d*-spacing of the highest diffractions was observed in TEM analysis. Fig. S2

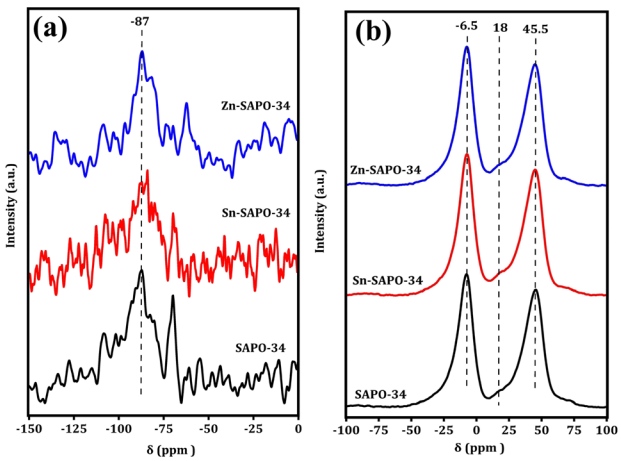

Fig. 3 ^{29}Si MAS NMR (a) and ^{27}Al MAS NMR (b) of SAPO-34 and modified SAPO-34 zeolites.

(ESI†) shows the homogeneous distribution of Mn, Zn, Zr, and O elements in the TEM-EDX elemental mappings.

The textural properties of the zeolites were investigated using the N_2 adsorption–desorption analysis and the isotherms are depicted in Fig. S3a (ESI†). The calculated BET surface area for SAPO-34 was 296 m^2 g^{-1}. However, the surface area decreased after the Zn and Sn introduction in SAPO-34. The calculated BET surface area for Zn-SAPO-34 and Sn-SAPO-34 was 274 m^2 g^{-1} and 249 m^2 g^{-1}, respectively. All the samples exhibited type IV isotherms with a H3 hysteresis loop and had an uptake of N_2 at a relative pressure of >0.5, overall suggesting the porous nature of the zeolites.

Acidic sites and their strength are crucial factors influencing the performance of zeolites in dehydration processes. In the NH_3 TPD analysis, all the zeolites displayed two desorption peaks: a notable desorption peak between 100 and 250 °C for weak acidic sites and another between 250–450 °C for medium acidic sites.[15] The first desorption peak is caused by weak acidic sites on the surface, such as hydroxyl groups. The second desorption peak is caused by the structural acidity of the molecular sieve framework, which contains the primary active sites for the MTO process.[16] As shown in Fig. S3b (ESI†), the relative desorption of the medium acidic sites compared to weak acidic sites decreased in the following order; SAPO-34 < Zn-SAPO-34 < Sn-SAPO-34. This implies that the medium acidic sites were slightly consumed after the Sn and Zn incorporation.[17]

The ^{29}Si and ^{27}Al MAS NMR spectra were recorded to investigate the coordination of these ions into the structural framework of SAPO-34 (Fig. 3a and b). The ^{29}Si NMR of all samples shows an intense signal near −87 ppm for the Si (4Al) species. This implies that all the samples possess relatively low silicon content because silicon-rich materials often display several peaks in this region.[16] In ^{27}Al NMR, all samples have an intense peak at 45.5 ppm, indicating the presence of tetrahedrally coordinated framework Al species. The peak with similar intensity at −6.5 ppm can be related to the six coordinated or octahedrally coordinated extra-framework Al atoms. The penta-coordinated Al atom, which exhibits a weak signal at 18 ppm, can be formed by the tetrahedral Al coordinating with one water molecule.[18]

The oxidation states and surface composition of the different components present in the Mn–Zn–Zr/Zn-SAPO-34 catalyst were detected using X-ray photoelectron spectroscopy. The XPS spectra of the Mn, Zn, Zr, Si, Al, and P elements are shown in Fig. S4 (ESI†).

The activity of the different zeolite catalysts for the methanol-to-olefins reaction is presented in Fig. S5 (ESI†). After that, the activity of the mortar mixed ZnO–ZrO_2 based-oxides and Zn-SAPO-34 for CO_2 hydrogenation to short-chain olefins *via* the methanol methanol-mediated route (CTM + MTO) was tested, and results are displayed in Fig. 4. The Zn–Zr/Zn-SAPO-34 bi-functional catalyst exhibited 10% CO_2 conversion with 82% CO selectivity and 18% hydrocarbons. In the hydrocarbon distribution, the selectivity of short-chain olefins and C_2–C_3 olefins was 85.7% and 65.6%, respectively, along with 2.1% CH_4 selectivity. The In–Zn–Zr/Zn-SAPO-34 and Mn–Zn–Zr/Zn-SAPO-34 catalysts exhibit enhanced CO_2 conversion with decreased CO selectivity without much affecting the hydrocarbon distribution. For the In–Zn–Zr/Zn-SAPO-34 and Mn–Zn–Zr/Zn-SAPO-34 catalysts, the CO_2 conversion was 13 and 18% with 72 and 65% CO selectivity, respectively. With this conversion, the short-chain olefin selectivity for the In–Zn–Zr/Zn-SAPO-34 and Mn–Zn–Zr/Zn-SAPO-34 catalysts was 81.9 and 81% with CH_4 selectivity of 3.2 and 3.9%, respectively (a detailed comparison with previously reported work is tabulated in Table S1, ESI†). The Mn–Zn–Zr/Zn-SAPO-34 catalyst was also tested for syn-gas (H_2 : CO ratio of 2 : 1) conversion to short-chain olefins *via* the methanol methanol-mediated route (STM + MTO). As shown in Fig. S6 (ESI†), the CO conversion obtained was 13% along with 83% short-chain olefin selectivity (CO_2 free).

The effect of Zn in Zn-SAPO-34 and Mn in Mn–Zn–Zr-based oxides on catalytic performance was also investigated and the results are demonstrated in Fig. S7a and S7b (ESI†).

Finally, the influence of the integration manner of the Mn–Zn–Zr with the Zn-SAPO-34 was analyzed and the results are shown in Fig. S8 (ESI†). It was found that the catalytic activity of mortar mixing followed by pelletization was superior to separate pelletization and subsequent mixing.

The Mn–Zn–Zr/Zn-SAPO-34 catalyst was studied using *in situ* DRIFTS to unravel the reaction pathways (Fig. S9, ESI†).

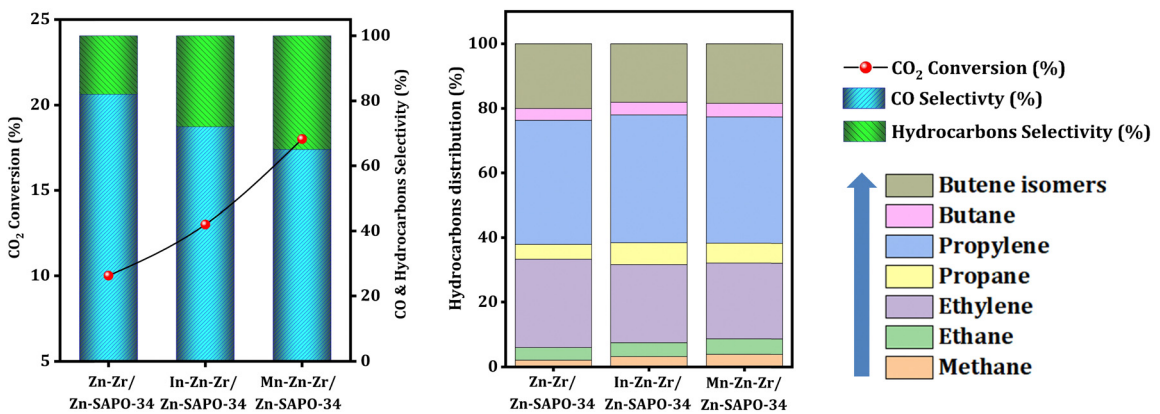

Fig. 4 The activity of ZnO–ZrO_2-based oxides admixed with Zn-SAPO-34 catalyst for direct CO_2 hydrogenation.

After 15 minutes of CO_2 adsorption, peaks are observed in the range of 2200–2400 cm^{-1}, corresponding to gas-phase CO_2, along with overtones between 3500–3800 cm^{-1}. Furthermore, the peaks observed at 1046, 1175, 1344, 1526, and 1631 cm^{-1} can be assigned to various carbonate species.[19] After He purging, the gas-phase CO_2 peaks disappeared, while the peaks corresponding to carbonate species remained intact. However, when the gas was switched to a CO_2 + H_2 mixture, peaks emerging at 1310 and 1578 cm^{-1} indicate uni-dentate and bidentate formate species, respectively.[20] Notably, after 10 minutes, the spectra showed no signals associated with methoxy species or gas-phase CO. However, by 20 minutes, new peaks became evident at 1084 cm^{-1}, attributed to methoxy species,[21] alongside distinct peaks at 2179 and 2107 cm^{-1}, corresponding to gas-phase CO.[22] The appearance of formate first, followed by methoxy groups and gas-phase CO species, confirmed the formate pathway for the methanol formation during the reaction, as illustrated schematically in Fig. S10 (ESI†).[23]

Modifying the SAPO-34 zeolites with the 3D transition metal series (Zn, Mn, *etc.*) is a common strategy.[24,25] The acid and diffusion properties of zeolite significantly influence the methanol conversion and product distribution. The MTO reaction is a shape-selective, acid-catalyzed reaction. It is generally acknowledged that the amount of acid sites on the catalyst surface and the catalyst's structural integrity significantly impact the methanol conversion. The NH_3 TPD study of the SAPO-34 and Zn-SAPO-34 revealed that the medium acidic sites of the SAPO-34 decreased in Zn-SAPO-34, indicating that the alteration of the SAPO-34 by Zn somewhat lowered the acidic characteristics of the SAPO-34 (Fig. S3b, ESI†). It is commonly known that a decrease in the medium acid site promotes the synthesis of ethene and propene by obstructing the hydrogen transfer and polymerization events that consume alkenes.[26] Similar results were shown in the present study, where we found that the Zn-modified SAPO-34 zeolites contain less strong acid sites, increasing the selectivity of ethene and propene.

The ZnO–ZrO_2 binary oxide catalyst system is frequently used for high-temperature CO_2 hydrogenation to synthesize methanol.[27,28] Nonetheless, a common tactic is to modify them using a third oxide to increase CO_2 conversion and minimize CO selectivity in the products.[29] Here, Mn oxide-modified ZnO–ZrO_2 oxides improve the CO_2 conversion and decrease the CO selectivity. In the case of ZnO–ZrO_2, the CO_2 conversion was around 10% with 82% CO selectivity. However, after Mn incorporation into ZnO–ZrO_2, the CO_2 conversion increased significantly to 18% with 65% CO selectivity. The strong basic characteristic of Mn can raise the C/H ratio over the catalyst surface, enhancing CO_2 conversion and lowering CO selectivity, which can account for the observed effects following Mn integration.[30]

In summary, we prepared different modified ZnO–ZrO_2 based-oxides and modified SAPO-34 catalysts and investigated them for direct CO_2 hydrogenation to short-chain olefins *via* a methanol-mediated route. Among the various oxide composites, Mn–Zn–Zr oxide mortar mixed with Zn-SAPO-34 catalyst displayed short-chain olefin selectivity of 81% (23.5% ethylene + 39.1% propylene + 18.4% butenes) in hydrocarbons, with around 3.9% CH_4 and a CO_2 conversion of 18%. The same catalyst was also investigated for the syngas conversion and displayed 13% CO conversion with 83.2% short-chain olefins (25.4% ethylene + 38.5% propylene + 19.3% butenes) and 3.6% CH_4 selectivity in hydrocarbons.

GS: writing – original draft, investigation. SP: formal analysis, investigation, VKS: investigation, and data curation. AB: writing – review, supervision, funding acquisition, conceptualization.

GS sincerely acknowledges the University Grants Commission (UGC) India, for providing the Fellowship. AB expresses his gratitude to CSIR-India (HCP-48) for the research grant.

Data availability

All data obtained in this study are included in this article.

Conflicts of interest

There are no conflicts to declare.

Notes and references

1 S. Fawzy, *et al.*, *Environ. Chem. Lett.*, 2020, **18**, 2069–2094.
2 Z. Gholami, *et al.*, *Energies*, 2021, **14**, 8190.
3 M. Ronda-Lloret, *et al.*, *ChemSusChem*, 2019, **12**, 3896–3914.
4 S. Yang, *et al.*, *RSC Adv.*, 2019, **9**, 14176–14187.
5 S. Saeidi, *et al.*, *Prog. Energy Combust. Sci.*, 2021, **85**, 100905.
6 P. S. Murthy, *et al.*, *Energy Fuels*, 2021, **35**, 8558–8584.
7 Y. Wei, *et al.*, *Mol. Catal.*, 2022, **525**, 112354.
8 X. Li, *et al.*, *Ind. Eng. Chem. Res.*, 2018, **57**, 1446–1453.
9 N. Najafi, *et al.*, *Powder Technol.*, 2014, **254**, 324–330.
10 Y. Peng, *et al.*, *Powder Technol.*, 2013, **233**, 325–330.
11 G. Singh, *et al.*, *ACS Sustainable Chem. Eng.*, 2023, **11**, 11181–11198.
12 M. C. Uribe López, *et al.*, *J. Nanomater.*, 2019, 1015876.
13 J. Wang, *et al.*, *Sci. Rep.*, 2016, **6**, 35020.
14 L. Wang, *et al.*, *J. Catal.*, 2015, **324**, 98–106.
15 A. M. Prakash, *et al.*, *J. Chem. Soc., Faraday Trans.*, 1994, **90**, 2291–2296.
16 F. Gong, *et al.*, *New J. Chem.*, 2020, **44**, 10410–10417.
17 Z. Wu, *et al.*, *Res. Chem. Intermed.*, 2019, **45**, 1309–1325.
18 L. Yang, *et al.*, *Nat. Commun.*, 2021, **12**, 4661.
19 E.-M. Köck, *et al.*, *J. Phys. Chem. C*, 2013, **117**, 17666–17673.
20 S. M. Fehr, *et al.*, *ChemCatChem*, 2022, **14**, e202101500.
21 L. Zhang, *et al.*, *Appl. Catal., A*, 2023, **657**, 119141.
22 L. Yao, *et al.*, *J. Catal.*, 2019, **372**, 74–85.
23 L. Lin, *et al.*, *ChemistrySelect*, 2021, **6**, 2119–2125.
24 H. Huang, *et al.*, *Catal. Sci. Technol.*, 2019, **9**, 2203–2210.
25 C. Pang, *et al.*, *RSC Adv.*, 2017, **7**, 32146–32154.
26 D. Chen, *et al.*, *Microporous Mesoporous Mater.*, 2012, **164**, 239–250.
27 J. Wang, *et al.*, *Sci. Adv.*, 2017, **3**, e1701290.
28 Y. Yang, *et al.*, *React. Kinet., Mech. Catal.*, 2022, **135**, 2993–3005.
29 Y. Wang, *et al.*, *Nat. Commun.*, 2019, **10**, 1166.
30 G. Singh, *et al.*, *Appl. Surf. Sci.*, 2023, 156401.